A Vector Hysteresis Current Control Applied on Three-Level Inverter. Application to the Active and Reactive Power Control of Doubly Fed Induction Generator Based Wind Turbine

T. Ghennam, E.M. Berkouk, B. Francois

Abstract – *This paper presents a new vector hysteresis current control (V.H.C.C), which is applied on a three-phase three-level voltage source inverter (VSI). The proposed control technique is used to control the active and reactive power of wind turbines by means of controlling the rotor currents of the doubly fed induction generator (DFIG). It gathers the three current errors into a single space vector quantity. In this case, the magnitude of the error vector is limited within boundary areas of a square shape and also the line current interactions are avoided in the three phase system. Furthermore, the application of the three zero voltage vectors reduces the mean switching frequency of the three phase three-level inverter.*

Keywords: *Vector hysteresis current control, three-phase three-level inverter, doubly fed induction generator, wind energy, active and reactive power control.*

Nomenclature

v_{sd}, v_{sq}	*d-q* stator voltage components;
i_{sd}, i_{sq}	*d-q* stator current components;
ϕ_{sd}, ϕ_{sq}	*d-q* stator flux components;
v_{rd}, v_{rq}	*d-q* rotor voltage components;
i_{rd}, i_{rq}	*d-q* rotor current components;
ϕ_{rd}, ϕ_{rq}	*d-q* rotor flux components;
$v_{r\alpha}, v_{r\beta}$	α - β rotor voltage components;
$i_{r\alpha}, i_{r\beta}$	α - β rotor current components;
e_{α}, e_{β}	α - β error current components;
P_s, Q_s	active and reactive power at the stator side;
ω_s	stator angular frequency;
ω_r	rotor angular frequency;
T	electromagnetic torque;
R_s	stator resistance;
L_s	stator inductance;
R_r	rotor resistance;
L_r	rotor inductance;
L_m	mutual inductance;
p	number of pole pairs;

I. Introduction

Because of the increasing rate of pollution and degradation of the environmental conditions, wind energy is becoming one of the most important renewable energy sources in European countries, US, and Asia. It could play a key role in solving the worldwide energy crisis, especially after the increases of the fuel prices during 1970's [1]. Due to its freely available, clean and renewable character, it can take a large part in electricity production.

Over the past decade, the installed wind power capacity in the world has been increasing more than 30% [2], [3]. Nowadays, the market for variable speed wind turbines is oriented to the design of high power wind generation systems (1 MW and more).

The electronic interface dealing with wind generator control is basically a back-to-back two-level converters; however this kind of power converter is seldom used for high power applications.

As a result, multilevel converters using pulse-width modulation are being increasingly preferred for high power applications [4], [5] such as wind power generation. The multilevel structure not only increases the power rating but also reduces stress across the switches and improves the voltage waveforms with lower harmonic content. The most popular structure of the multi-level voltage source inverter (VSI) is the neutral point clamped converter (NPC) proposed in 1981 by Nabae and al [4].

In order to control inverter currents, many contributions have been done in recent decades. The

Manuscript received January 2007, revised January 2007

classifications of current controllers have been presented in [6]-[8]. Among them three classes of controllers have been developed: hysteresis controllers, linear PI controllers and predictive dead-beat controllers [9]. The current control using three independent hysteresis comparators is widely used due to its simple implementation. Moreover, beside the fast dynamic response, it does not require any knowledge of the load parameters [6], [9]-[11]. However the limit cycle oscillations, random switching and phase current interactions [8], [13] and [14] have been considered as the main drawbacks of the conventional hysteresis controllers.

Recent works [14]-[17] are focused on the hysteresis current controllers for multilevel drives, but only for single-phase multilevel inverters.

In this paper, a new vector hysteresis current control (V.H.C.C) is presented, for three phase three-level VSI. This three-level VSI supplies a rotor winding of the doubly fed induction generator (DFIG). The proposed control technique controls the active and reactive powers of the wind turbine based on the DFIG by controlling its rotor currents. In contrast to the conventional hysteresis where the three independent current errors are used, the control scheme gathers them into a single space vector quantity. In this case the magnitude of the error vector is limited within boundary areas of a square shape. Moreover the line current interactions are avoided in the three phase system and the application of the three zero voltage vectors reduces the switching frequency of the three phase three-level VSI. The control strategy is theoretically explained and verified by simulations.

II. Description of the wind energy conversion system

A simplified diagram of the wind energy conversion system is illustrated in figure 1. It consists of a wind turbine, a gearbox, a DFIG, and back-to-back three-level converters. The stator winding of the DFIG is directly connected to the grid, whereas the rotor winding is fed by back-to-back three-level PWM converters. The grid side converter is connected to the grid via three chokes to improve the current harmonic distortion. The rotor side converter controls the power flow to the grid by controlling the rotor currents of the DFIG. The direct and quadrature rotor current components allow a decoupled control of active and reactive powers. The quadrature current component controls the active power, whereas the direct current component controls the reactive power.

The presented work focuses only on the control of the rotor side converter.

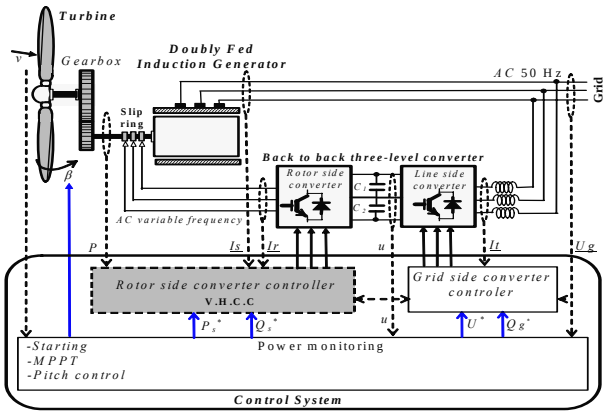

Fig. 1. Simplified diagram of the wind conversion system

III. Dynamic model of the doubly fed induction machine

A commonly used model for the doubly fed induction machine (DFIM) is the Park model. The electrical equations of the DFIM in the Park reference frame are given as follows [18], [19]:

$$\begin{cases} v_{sd} = R_s i_{sd} + \dfrac{d\phi_{sd}}{dt} - \omega_s \phi_{sq} \\ v_{sq} = R_s i_{sq} + \dfrac{d\phi_{sq}}{dt} + \omega_s \phi_{sd} \end{cases} \quad (1)$$

$$\begin{cases} v_{rd} = R_r i_{rd} + \dfrac{d\phi_{rd}}{dt} - \omega_r \phi_{rq} \\ v_{rq} = R_r i_{rq} + \dfrac{d\phi_{rq}}{dt} + \omega_r \phi_{rd} \end{cases} \quad (2)$$

The stator and rotor flux are given as:

$$\begin{cases} \phi_{sd} = L_s i_{sd} + L_m i_{rd} \\ \phi_{sq} = L_s i_{sq} + L_m i_{rq} \end{cases} \quad (3)$$

$$\begin{cases} \phi_{rd} = L_r i_{rd} + L_m i_{sd} \\ \phi_{rq} = L_r i_{rq} + L_m i_{sq} \end{cases} \quad (4)$$

In these equations, R_s, R_r, L_s and L_r are respectively the resistances and the inductances of the stator and the rotor windings, L_m is the mutual inductance.

$v_{sd}, v_{sq}, v_{rd}, v_{rq}, i_{sd}, i_{sq}, i_{rd}, i_{rq}, \phi_{sd}, \phi_{sq}, \phi_{rd}$ and ϕ_{rq} are the d and q components of the stator and rotor voltages, currents and flux, whereas ω_r is the rotor speed in electrical degree.

The electromagnetic torque is expressed as:

$$T = p(\phi_{sd} . i_{sq} - \phi_{sq} . i_{sd}) \quad (5)$$

Stator and rotor variables are both referred to the stator reference Park frame. With the following orientation, the *d* component of the stator flux is equal to the total flux whereas the *q* component of the stator flux is null (Fig. 4.a).

$$\phi_{sd} = \phi_s, \phi_{sq} = 0 \tag{6}$$

By replacing (6) in (3) and (5), the electromagnetic torque can be given as follows:

$$T = p\frac{L_m}{L_s} i_{rq} \phi_{sd} \tag{7}$$

Assuming that the resistance of the stator winding R_s is neglected, and referring to the chosen reference frame, the voltage equations and the flux equations of the stator winding can be simplified in steady state as follows:

$$\begin{cases} v_{sd} = 0 \\ v_{sq} = v_s = \omega_s \phi_s \end{cases} \tag{8}$$

$$\begin{cases} \phi_s = L_s i_{sd} + L_m i_{rd} \\ 0 = L_s i_{sq} + L_m i_{rq} \end{cases} \tag{9}$$

From (9), the equations linking the stator currents to the rotor currents are deduced below:

$$\begin{cases} i_{sd} = \dfrac{\phi_s}{L_s} - \dfrac{L_m}{L_s} i_{rd} \\ i_{sq} = -\dfrac{L_m}{L_s} i_{rq} \end{cases} \tag{10}$$

The active and reactive powers at the stator side are defined as:

$$\begin{cases} P_s = v_{sd} i_{sd} + v_{sq} i_{sq} \\ Q_s = v_{sq} i_{sd} - v_{sd} i_{sq} \end{cases} \tag{11}$$

Tacking into consideration the chosen reference frame, the above power equations can be written as follows:

$$\begin{cases} P_s = v_s i_{sq} \\ Q_s = v_s i_{sd} \end{cases} \tag{12}$$

Replacing the stator currents by their expressions given in (12), the equations below are obtained:

$$\begin{cases} P_s = -v_s \dfrac{L_m}{L_s} i_{rq} \\ Q_s = \dfrac{v_s \phi_s}{L_s} - \dfrac{v_s L_m}{L_s} i_{rd} \end{cases} \tag{13}$$

The block diagram of the DFIG model in Park reference frame is depicted in figure 2, assuming a constant stator voltage (v_s).

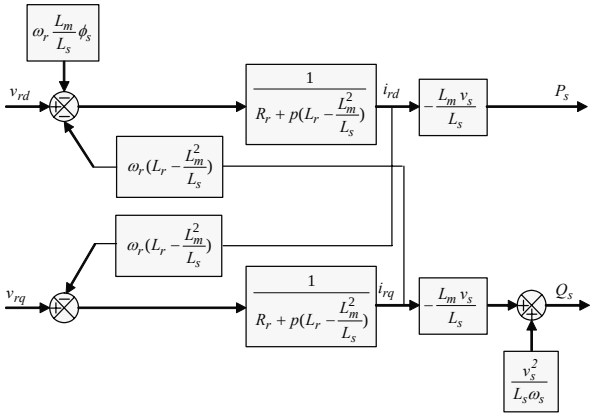

Fig. 2. Block diagram of the DFIM model

IV. The proposed vector hysteresis current control (V.H.C.C)

IV.1. Control of the rotor side converter

The block diagram of the rotor side converter control is shown in figure 3. The active and reactive powers are compared to their references, and then two PI controllers are used. The outputs of the two PI controllers represent the direct and quadrature components of the current references. The rotor currents of the DFIG are compared to their references after being sensed and transformed to $\alpha\beta$ reference frame using equation (14). The two DC capacitors, which supply the three-level VSI, are assumed with great value in order to neglect the DC capacitor unbalance.

$$\begin{bmatrix} i_{r\alpha}^* \\ i_{r\beta}^* \end{bmatrix} = \sqrt{\frac{2}{3}} \begin{bmatrix} 1 & -\frac{1}{2} & -\frac{1}{2} \\ 0 & \frac{\sqrt{3}}{2} & \frac{-\sqrt{3}}{2} \end{bmatrix} \begin{bmatrix} i_{ra} \\ i_{rb} \\ i_{rc} \end{bmatrix} \tag{14}$$

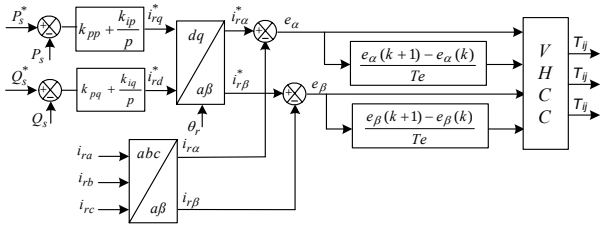

Fig. 3. Block diagram of the rotor side converter control

The electrical rotor angle θ_r is defined by the angle between the rotor axis and the d axis (Fig. 4.a). It is computed by using the electrical stator angle θ_s and the mechanical angle θ_m as it is shown in figure 4.b.

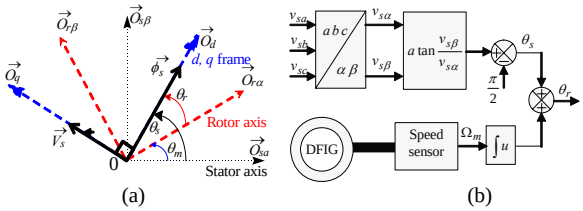

Fig. 4. Determination of the electrical angles in Park reference frame.

IV.2. Three-phase three-level voltage source inverter

The three phase three-level VSI has three switching commutation cells; each one contains four IGBT and two neutral clamping diodes (Fig. 5).

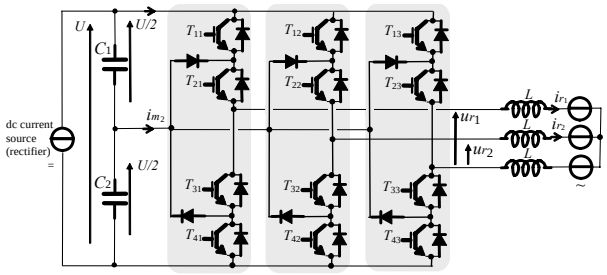

Fig. 5. Three-phase three-level VSI

The voltage outputs of the three-level VSI can be expressed as follows:

$$\begin{bmatrix} v_{r1} \\ v_{r2} \end{bmatrix} = \frac{1}{3}\begin{bmatrix} 2 & -1 \\ -1 & 2 \end{bmatrix}\begin{bmatrix} u_{r1} \\ u_{r2} \end{bmatrix} \tag{15}$$

The voltage outputs of the three-level VSI can be written in the $\alpha\beta$ reference frame as follows:

$$\begin{bmatrix} v_{r\alpha} \\ v_{r\beta} \end{bmatrix} = \begin{bmatrix} \sqrt{3/2} & 0 \\ \sqrt{1/2} & \sqrt{2} \end{bmatrix}\begin{bmatrix} v_{r1} \\ v_{r2} \end{bmatrix} \tag{16}$$

The 27 possible combinations of switching states result in 27 voltage vectors. Among them three are zero voltage vectors (ZVV) ($\vec{v}_0, \vec{v}_7, \vec{v}_{14}$), and 24 are non-zero voltage vectors (NZVV). The proposed control strategy requires only 21 voltage vectors shown in figure 6 since the six redundant inverter switching states are not used.

The small hexagon figure 6.b is defined by the six vectors ($\vec{v}_1, \vec{v}_2, \vec{v}_3, \vec{v}_4, \vec{v}_5, \vec{v}_6$), all these vectors have the same magnitude $E/\sqrt{6}$. The medium hexagon figure 6.c is defined by the six vectors ($\vec{v}_8, \vec{v}_9, \vec{v}_{10}, \vec{v}_{11}, \vec{v}_{12}, \vec{v}_{13}$), all vectors have the same magnitude $E/\sqrt{2}$. The large hexagon figure 6.d is defined by the six vectors ($\vec{v}_{15}, \vec{v}_{16}, \vec{v}_{17}, \vec{v}_{18}, \vec{v}_{19}, \vec{v}_{20}$), these vectors have the same magnitude $E\sqrt{2}/\sqrt{3}$.

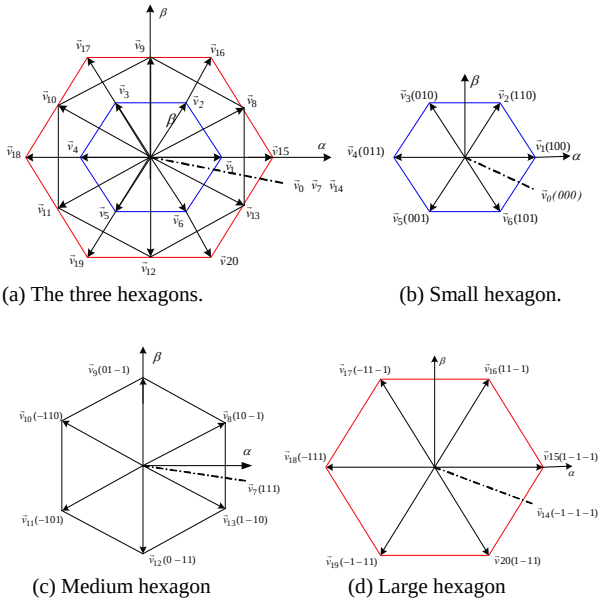

(a) The three hexagons. (b) Small hexagon.

(c) Medium hexagon (d) Large hexagon

Fig. 6. Three-level voltage inverter vectors in $\alpha\beta$ frame

IV.3. Principle of the proposed hysteresis control

The reference current and the measured rotor current of the DFIG can be both expressed using the space vector representation as follows:

$$\begin{cases} \bar{i}_r^* = i_{r\alpha}^* + j i_{r\beta}^* \\ \bar{i}_r = i_{r\alpha} + j i_{r\beta} \end{cases} \tag{17}$$

By the same way, the error vector defined by $\bar{e} = \bar{i}_r^* - \bar{i}_r$ can be given in $\alpha\beta$ reference frame by the following expression:

$$\bar{e} = e_\alpha + j e_\beta \tag{18}$$

The tip of the reference current vector $\vec{i}_r^*$ is located in the center of area A_I. The tip of the measured current vector $\vec{i}_r$ can be located in one of the fourth areas (A_I, A_{II}, A_{III}, A_{IV}), according to the three hysteresis bands h_1, h_2, h_3, as it is illustrated in figure 7

Table I gives the membership conditions of the error vector tip to the four possible areas.

TABLE I
MEMBERSHIP CONDITIONS OF THE ERROR VECTOR TIP TO THE FOUR AREAS

Conditions	Areas
$\lvert e_\alpha \rvert < h_1/2 \,\&\, \lvert e_\beta \rvert < h_1/2$	A_I
$h_1/2 < \lvert e_\alpha \rvert < h_2/2 \,\&\, h_1/2 < \lvert e_\beta \rvert < h_2/2$	A_{II}
$h_2/2 < \lvert e_\alpha \rvert < h_3/2 \,\&\, h_2/2 < \lvert e_\beta \rvert < h_3/2$	A_{III}
$\lvert e_\alpha \rvert > h_3/2 \,\&\, \lvert e_\beta \rvert > h_3/2$	A_{IV}

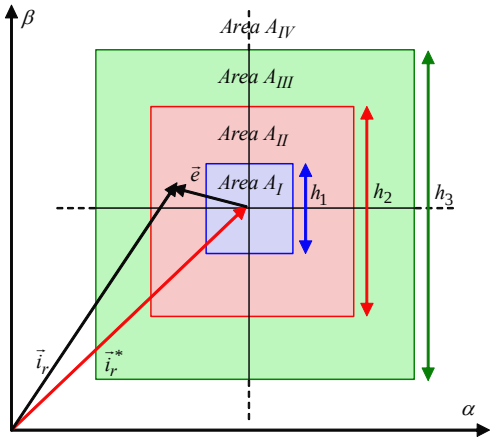

Fig. 7.The four possible areas of the error vector tip

As it is displayed in figure 8, the three areas A_I, A_{II} and A_{III} are limited by hysteresis boundaries h_1, h_2, h_3, and area A_{IV} has no up limit $(x > h_3/2)$. Each of the three areas A_{II}, A_{III} and A_{IV} is divided into four sectors. Area A_I represents one sector, which is named S_5. The sectors are numbered from 1 to 13. Figure 8 shows an example of one sector from each area. The error vector tip can be located in one of the thirteen sectors, according to the sign of α, β components of the error vector. Table II gives the membership conditions of the error vector tip to the thirteen possible sectors.

TABLE II
MEMBERSHIP CONDITIONS OF THE ERROR VECTOR TIP TO THE THIRTEEN SECTORS

e_α \ Areas / e_β	A_I	A_{II}	A_{III}	A_{IV}
- -	S_5	S_1	S_6	S_{10}
+ -	S_5	S_2	S_7	S_{11}
- +	S_5	S_3	S_8	S_{12}
+ +	S_5	S_4	S_9	S_{13}

Once the sector is determined, one among the 21 voltage vectors must be applied to push the rotor currents of the DFIG to their references within the hysteresis boundaries. The suitable choice of the voltage vectors depends mainly on the location of the error vector tip (Fig. 8).

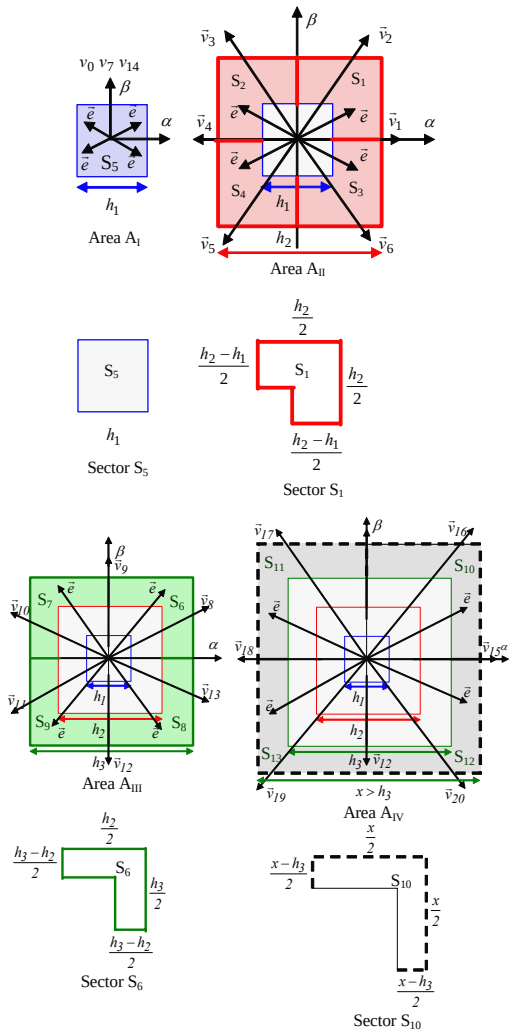

Fig. 8. Error vector tip location in the thirteen possible sectors

In the case where the error vector tip is located in the area A_{II}, one of the small hexagon voltage vectors will be applied. By the same way, if the error vector tip is located in the area A_{III}, one of the medium hexagon voltage vectors will be selected. Otherwise, one among the large hexagon voltage vectors will be applied, if the error vector tip is located in the area A_{IV}.

To reduce the switching frequency, the ZVV must be applied. This will be carried out only when it is certain that the action of the rotor voltage vector has the natural tendency to push the error vector tip towards the hysteresis boundary areas. This can be easily verified by checking up both conditions:

$$\bar{e}_\alpha . \frac{d\bar{e}_\alpha}{dt} < 0 \quad \text{and} \quad \bar{e}_\beta . \frac{d\bar{e}_\beta}{dt} < 0 \qquad (19)$$

However, if conditions (19) are not verified, the selection of the NZVV must be done to reverse the natural tendency of the current error trajectory. In this case, the suitable NZVV has to drive the error vector toward hysteresis areas. For area A_I, the ZVV $(\bar{v}_o)$ is the appropriate voltage vector to be selected since it

keeps the error vector tip inside it. For other areas, the selection rule of the appropriate voltage vector follows the conditions (19).

To understand the selection rule of the appropriate voltage vector, in the three areas (A_{II}, A_{III}, and A_{IV}), the sector S_1 of area A_{II}, which corresponds to the case where both current error $\alpha\beta$ components are negative is taken as an example. Figure 9 and table III explain the selection rule for sector S_1. We denote that:

$$\frac{d\bar{e}_i}{dt} = 0 \text{ means } \frac{d\bar{e}_i}{dt} < 0$$
$$\frac{d\bar{e}_i}{dt} = 1 \text{ means } \frac{d\bar{e}_i}{dt} > 0 \qquad i = \alpha, \beta$$

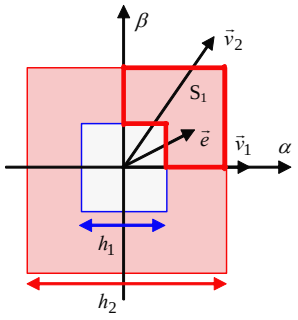

Fig. 9. Error vector tip location in sector S_1.

TABLE III
SWITCHING TABLE FOR SECTOR S_1

Case	$\frac{de_\alpha}{dt}$	$\frac{de_\beta}{dt}$	Applied Vector
1	0	0	V_2
2	1	0	V_2
3	0	1	V_1
4	1	1	ZVV

From table III:

1-For case 1, which corresponds to the increase of both α and β components, the appropriate voltage vector to move the error back to the hysteresis boundary is $\vec{v}_2$.

2-For case 2, which corresponds to the decrease of α component and the increase of β component, the voltage vector $\vec{v}_2$ remains the best choice since there is no voltage vector that has an effect only on the α component.

3-For case 3, which corresponds to the increase of α component and to the decrease of β component, the voltage vector $\vec{v}_1$ is the best choice since it has an effect only on the α component. So $\vec{v}_1$ is applied only when the α component error is moving alone in the wrong way.

4-For case 4, which corresponds to the decrease of both α and β components, the error is naturally converging to the right direction and there is no need to apply the NZVV, so the ZVV is selected.

The selection between the three ZVV is determined in a way to minimise the switching frequency, by adopting the principle to switch only one inverter leg at once. Tables IV, V, VI and VII display the switching tables for each sector in areas A_I, A_{II}, A_{III} and A_{IV} respectively.

TABLE IV
SWITCHING TABLE FOR AREA A_I

$\frac{de_\alpha}{dt}$	$\frac{de_\beta}{dt}$	S_5
0	0	ZVV
1	0	ZVV
0	1	ZVV
1	1	ZVV

TABLE V
SWITCHING TABLE FOR AREA A_{II}

$\frac{de_\alpha}{dt}$	$\frac{de_\beta}{dt}$	S_1	S_2	S_3	S_4
0	0	V_2	V_3	V_1	ZVV
1	0	V_2	V_3	ZVV	V_4
0	1	V_1	ZVV	V_6	V_5
1	1	ZVV	V_4	V_6	V_5

TABLE VI
SWITCHING TABLE FOR AREA A_{III}

$\frac{de_\alpha}{dt}$	$\frac{de_\beta}{dt}$	S_6	S_7	S_8	S_9
0	0	V_8	V_9	V_{13}	ZVV
1	0	V_9	V_{10}	ZVV	V_{11}
0	1	V_8	ZVV	V_{13}	V_{12}
1	1	ZVV	V_{10}	V_{12}	V_{11}

TABLE VII
SWITCHING TABLE FOR AREA A_{VI}

$\frac{de_\alpha}{dt}$	$\frac{de_\beta}{dt}$	S_{10}	S_{11}	S_{12}	S_{13}
0	0	V_{16}	V_{17}	V_{15}	ZVV
1	0	V_{16}	V_{17}	ZVV	V_{18}
0	1	V_{15}	ZVV	V_{20}	V_{19}
1	1	ZVV	V_{18}	V_{20}	V_{19}

V. Simulation results

The proposed V.H.C.C technique has been tested on a three phase three-level VSI, which supplies the rotor side of the DFIG. The delivered active and reactive powers from the wind turbine to the grid are controlled by means of controlling the rotor currents of the DFIG. The simulation of the overall system shown in figure 3 has been carried to verify the performances of the proposed control technique. All simulation results are obtained at a fixed speed of the DFIG (1624*rpm*), a fixed hysteresis bands (h_1=*0.45*, h_2=*0.47*, h_3=*0.49*) and a *600 V*DC bus.

Active reactive power references are respectively set to P_s^* = *-2 kW*, Q_s^* = *0 VAR*.

The simulation parameters of the DFIG are:

Nominal power: *7.5 kW*, nominal speed *1500 rpm*, pairs of pole number: *p=2*, inertial: *0.3125Kg.m2*, viscous coefficient: *6.73.10e-3N.m.s*$^{-1}$, stator resistance:

R_s=0.455 Ω, stator inductance: L_s=0.084H, rotor resistance: R_r=0.062 Ω, rotor inductance: L_r=0.081H, mutual inductance: L_m=0.078.

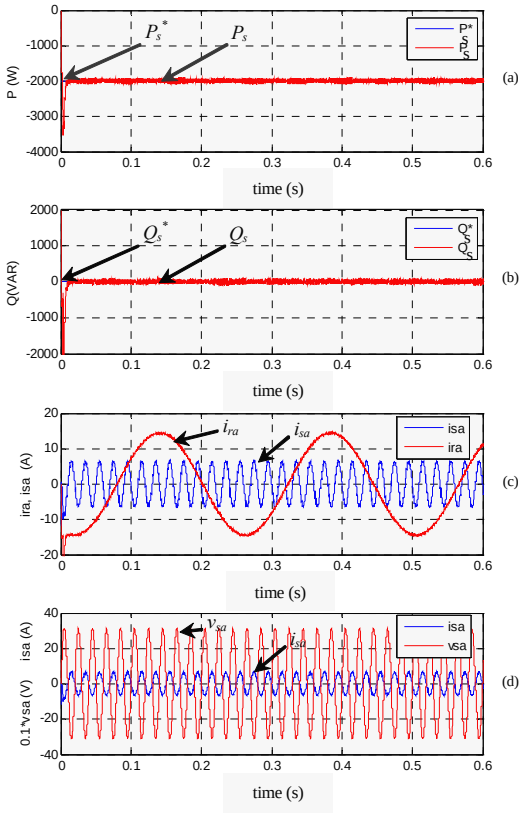

Fig. 10. Simulation waveforms of the V.H.C.C applied on the rotor side three-level converter
(a) Reference and measured active powers of the DFIG.
(b) Reference and measured reactive powers of the DFIG.
(c) Rotor and stator currents of the DFIG.
(d) Supply voltage and stator current of the DFIG.

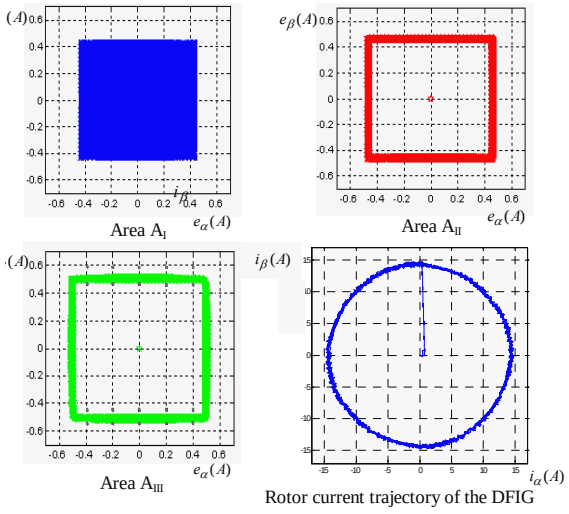

Fig. 11. Current error trajectory in the three areas A_I, A_{II} and A_{III} And the rotor current trajectory of the DFIG

Figure 10 illustrates the simulation waveforms of the system shown in figure 3. It is clearly shown from figures 10.a and 10.b, that the active and reactive powers of the DFIG follow respectively their references.

Figure 10.c illustrates the stator and rotor currents of the DFIG. It is obvious, that the rotor current frequency is lower than the stator current frequency. It is clearly denoted from figure 10.d, that the stator current and the supply voltage are in π phase, hence the DFIG injects an active current to the grid.

Figure 11 shows the current error trajectory in area A_I, A_{II} A_{III} and A_{IV} and also the rotor current trajectory of the DFIG, which is circular in the $\alpha\,\beta$ plane.

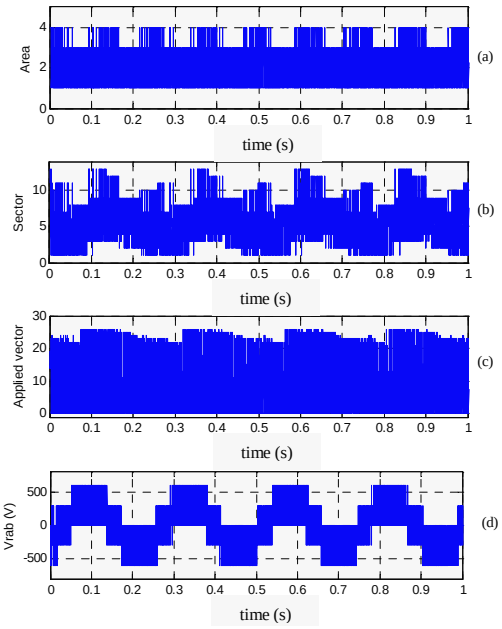

Fig. 12. Simulation waveforms of:
(a) Areas in which the error vector tip can be located.
(b) Sectors in which the error vector tip can be located.
(c) The applied vector.
(d) One phase-to-phase voltage of the DFIG rotor

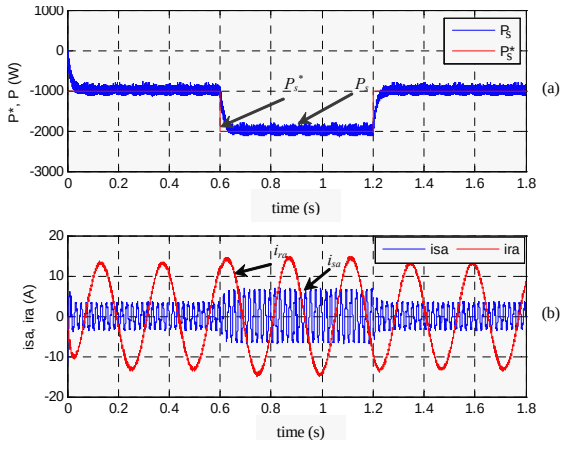

Fig. 13. Simulation waveforms in case of a step-change in the active power
(a) Reference and measured active powers of the DFIG.
(b) Rotor and stator currents of the DFIG.

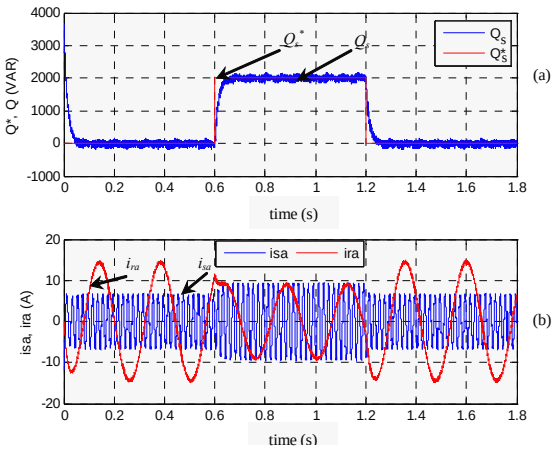

Fig .14. Simulation waveforms in case of step-change in the reactive power.
(a) Reference and measured reactive powers of the DFIG.
(b) Rotor and stator currents of the DFIG.

Figures 12.a and 12.b display the area and the sector in which the error vector tip can be located, whereas the applied voltage vector is shown in figure 12.c. The phase-to-phase voltage of the three-level VSI is shown in figure 12.d.

Figures 13 and 14 show the simulation waveforms with step changes in active and reactive power respectively. It is obvious from figures 13.b and 14.b that the active and reactive power control is directly linked to the control of the DFIG rotor currents.

VI. Conclusion

For controlling the active and reactive powers of the wind turbine based on doubly fed induction generator, a new vector hysteresis current control (V.H.C.C) has been presented in this paper. The control scheme is applied on a three-phase three-level VSI that supplies the rotor winding of the DFIG controlling by that its rotor currents.

The proposed control technique gathers the three current errors into a single space vector quantity. Hence the magnitude of the error vector is limited within a boundary area of a square shape, and also the line current interactions are avoided in the three phase system. Moreover, the application of the three zero voltage vectors reduces considerably the switching frequency.

The simulation results of the overall system with the proposed control technique show good performances.

References

[1] R.C. Bansal, T.S. Bhatti, D.P. Kothari, Bibliography on the application generators in non conventional energy systems, *IEEE Transaction on Energy Conversion, vol. 18 n. 3* September 2003.

[2] P. Gipe, Soaring to new heights: the world wind energy market, *Renewable Energy World, vol. 5. n. 4,* September/October 2002, pp.33-47.

[3] M. Jujawa, Large wind rising, *Renewable Energy World, vol. 6 n. 2*, Mars/April 2003, pp.39-51.

[4] A. Nabae, I. Takahashi, H. Akagi, A new neutral point clamped PWM inverter, *IEEE Transaction on Industrial Application*, *vol. 17,* 1981, pp. 518–523.

[5] H. Stemmler, P. Geggenbach, Configurations of high power voltage source inverter drives, *proceeding of the 5th European conference on power electronics and applications Vol. 5*, 1993, pp 7–12, Brighton, UK.

[6] M.P. Kazmierkoswki, L. Malesani, Current control techniques for three phase voltage source PWM converters: a survey, *IEEE Transaction on Industrial Electronics, vol. 45. n. 5*, 1998, pp. 691–703.

[7] I. Nagy, Novel adaptive tolerance band based PWM for field oriented control of induction machines, *IEEE Transaction on Industrial Electronics, vol. 41 no. 4,* 1994, pp. 406–417.

[8] D.M. Brod, D.W. Novotny, Current control of VSI-PWM inverters, *IEEE Transaction on Industrial Application, vol. 21 no. 4*, 1985, pp. 562–570.

[9] S. Buso, L. Malesani, P. Mattavelli, Comparison of Current Control Techniques for Active Filter Applications, *IEEE Transaction on Industrial Electronics*, *vol. 45, No.5*, October 1998, pp.722-729.

[10] S. Salama, S. Lennon, Overshoot and limit cycle free current control method for PWM inverters, *Proceeding of European Conference on Power Electronics and Applications (EPE),* pp. 3/247–251, 1991, Firenze, Italy

[11] B.H. Kwon, T.W. Kim, J.H. Youm, Novel SVM-based hysteresis current controller, *IEEE Transaction on Power Electronics, vol. 13 n. 2*, 1998, pp. 297–307.

[12] I. Nagy, Z. Suto, L. Backhausz, Periodic states of hysteresis current control of induction motor. *Proceeding of the 9th European Conf on Intelligent Motion (PCIM),* May 1996, pp. 605–619, Nurnberg, Germany.

[13] P.N. Tekwani, R.S. Kanchan, K. Gopakumar, Current-error space-vector-based hysteresis PWM controller for three-level voltage source inverter fed drives, *IEE Proceeding of Electric . Power Applications. Vol. 152, No. 5*, September 2005.

[14] M.R. Baiju, K. Gopakumar, L. Umanand, A. Pittet, Multi axis space phasor based multi level current hysteresis controller for an open-end winding induction motor fed from dual inverters, *Proceeding of the 29th European Conference on Intelligent Motion (PCIM)*, 2002, pp. 405–410, Nurnberg, Germany.

[15] G.H. Bode, D.N. Zmood, P.C. Loh, D.G. Holmes, A novel hysteresis current controller for multilevel single phase voltage source inverters, *Proceeding of IEEE Power Electronics Specialists Conference (PESC),* 2001, pp. 1845–1850.

[16] P.C. Loh, G.H. Bode, D.G. Holmes, T.A. Lipo, A time-based double band hysteresis current regulation strategy for single-phase multilevel inverters, *Proceeding of the IEEE-Industrial Applications Society, Annual Meeting*, 2002, pp. 1994–2001.

[17] K.A. Corzine, A hysteresis current–regulated control for multi-level drives, *IEEE transaction on energy conversion*, vol. 15, n. 2, 2000, pp. 169–175.

[18] S. EL Aimani, B. François, F. Minne, B. Robyns, Modelling and simulation of doubly fed induction generators for variable speed wind turbines integrated in a distribution network, *proceeding of the 10th European conference on power electronics and applications*, 2-4 September 2003, Toulouse, France.

[19] F. Poitiers, *Etude et commande de génératrices asynchrones pour l'utilisation de l'énergie éolienne*, thèse de doctorat de l'université de Nantes 19 Décembre 2003.

Authors' information

Tarak Ghennam was born in Ain Kercha, Oum El-Bouaghi, Algeria in 1977. He received his Engineering degree and master degree in 2000 and 2005 respectively in Electrical Engineering from the Polytechnic School of Algiers (ex: ENITA), Algeria. Since 2005, He has been a lecturer researcher in the electrical engineering department of the Polytechnic School of Algiers (ex: ENITA). His main research interests deal with the control techniques of multilevel converters used for renewable energy based power systems.

E.M. Berkouk was born in Algeria in 1968. He received his Engineering degree in 1991 in Electrical Engineering from the Polytechnic National School of Algiers, Algeria. In 1992 and 1995 he obtained, respectively, a Master of Science in ENSEEIHT (Toulouse) and Ph.D. in CNAM (Paris). From 1993 to 1996, he was teaching at the University of Paris XI. Since 1996, he is with the Polytechnic National school of Algiers as a Professor. His current research interests are power electronics, electrical drives and renewable energy.

Bruno Francois was born in St Amand les Eaux, France, 1969. He received the Ph. D. degree from the University of Lille, France in 1996. He is Associate Professor at the department of Electrical Engineering of Ecole Centrale de Lille. He is a member of Laboratory of Electrical Engineering (L2EP), Lille. He is currently working on the design of modulation and control systems for multilevel converters and also the development of renewable energy based power systems.